Supporting Information

Surface-anchored Carbon Nanomaterials for antimicrobial surfaces

L. Giraud[1], O. Marsan[1], E. Dague[2], Myriam Ben-Neji[3], C. Cougoule[3], E. Meunier[3], A. M. Galibert[1], A. Tourrette[1*] and E. Flahaut[1*]

[1]. CIRIMAT, Université Toulouse 3 Paul Sabatier, CNRS, INP Toulouse, Toulouse, France

[2]. LAAS-CNRS, Université de Toulouse, CNRS, Toulouse, France

[3]. Institute of Pharmacology and Structural Biology (IPBS), University of Toulouse, CNRS, Toulouse; France

The comparison of the C1s bands of raw and oxidized DWCNTs highlights the increase in the contribution of the sp^3 type carbon with oxidation, as well as the increase in the contribution of the carboxylic functions at 288.3 eV. In both cases, this band is very characteristic of a carbon mainly under sp^2 hybridization. This evolution of the oxygen content is all the more obvious when we look at the O1s band which intensity increases very strongly.

The differences in the carbon structural quality of the FLG and GO samples can clearly be distinguished by comparing the C1s band which widens and also shifts towards higher energies. The analysis of the O1s band reveal that oxygen represents only a very small proportion of the FLG sample (ca. 5 wt. %), while this element represents 30 wt. % in GO.

It should be noted that the analysis, in particular of the C1s band, is a delicate step. It is often the sp^2 carbon peak at 284.05 eV that is used to correct the energy spectra. Therefore, there are several possibilities to interpret the position of the C1s band in the case of GO, since the energy maximum is measured at 284.8 eV, which is normally the position of the sp^3 carbon. This would mean that the sp^2 carbon would be very much in the minority in the GO sample. It is possible to analyze the data differently by carrying out an energy readjustment (which amounts to repositioning the maximum of the signal at 284.05 eV), considering that the carbon remains mainly sp^2 since we maintain the 2D morphology. It is difficult in practice to provide very solid elements to justify one approach rather than another. This is the reason why we consider that it is not very reasonable to propose a much finer analysis of these data.

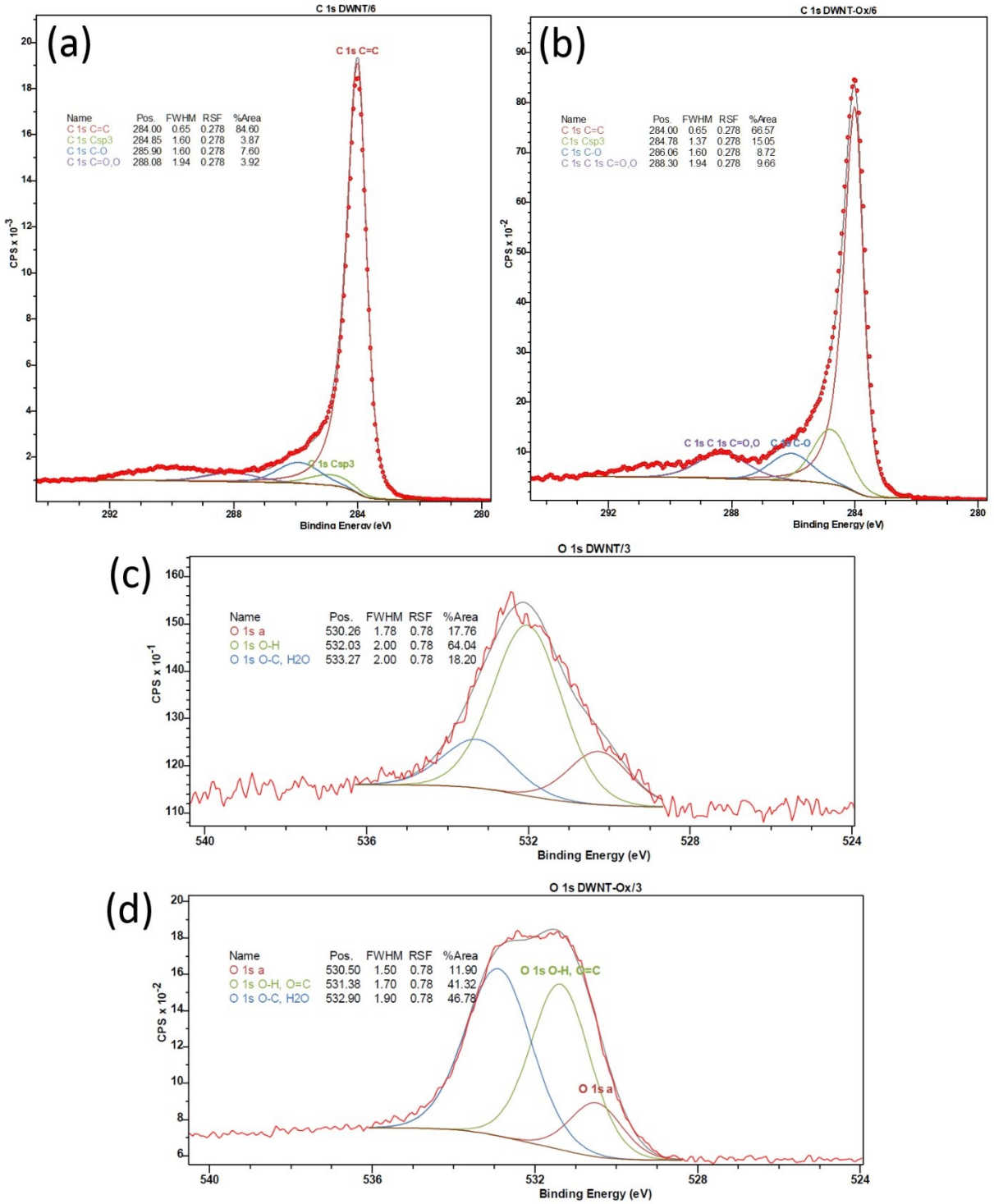

Figure S1: XPS analysis of DWCNTs (a, c) and DWCNTs Ox (b, d) : (a) C1s band of DWCNTs, (b) C1s band of DWCNTs Ox, (c) O1s band of DWCNTs, (d) O1s band of DWCNTs Ox

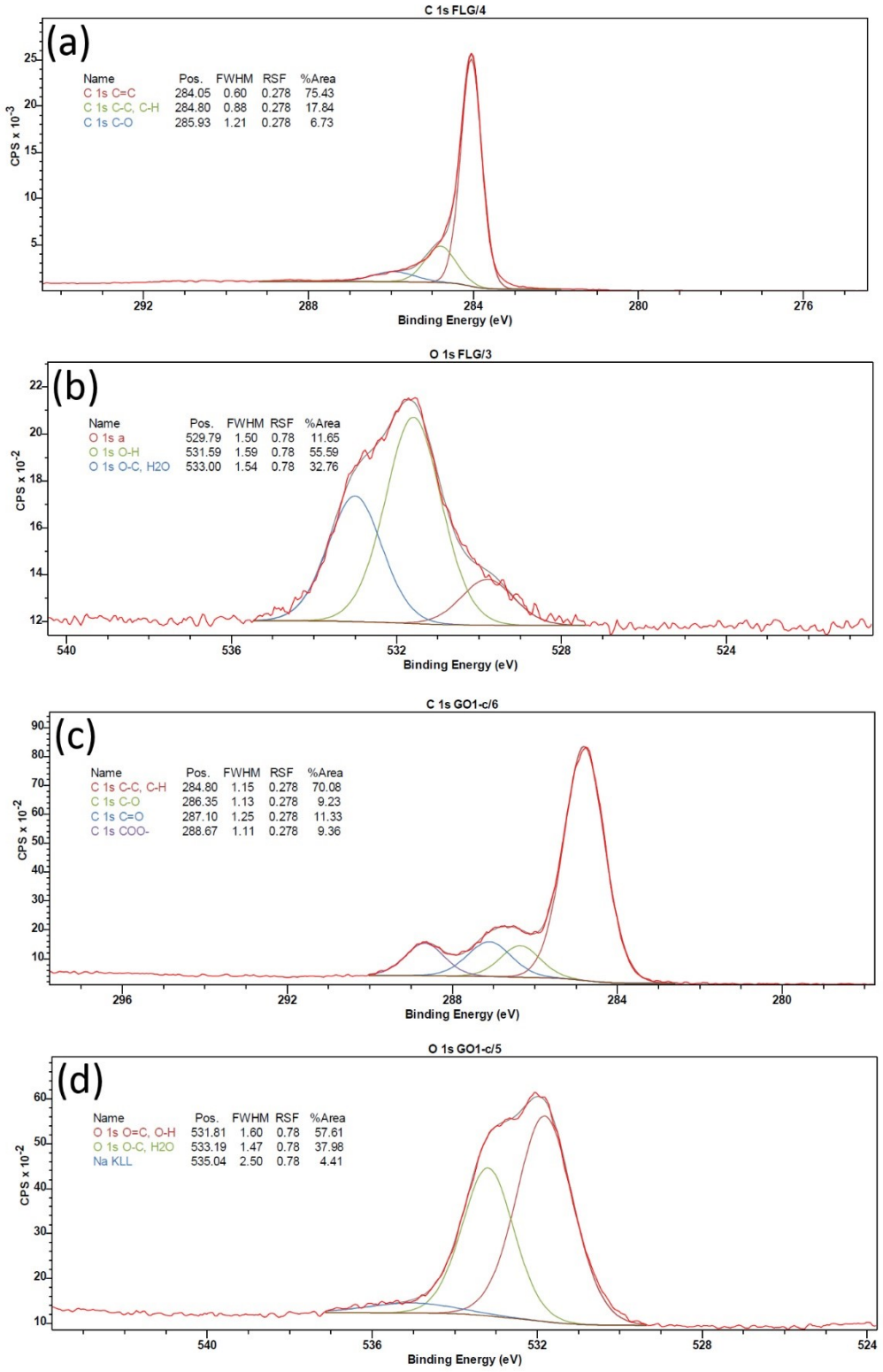

Figure S2: XPS analysis of FLG (a, c) and GO (b, d) : (a) C1s band of FLG, (b) C1s band of GO, (c) O1s band of FLG, (d) O1s band of GO.

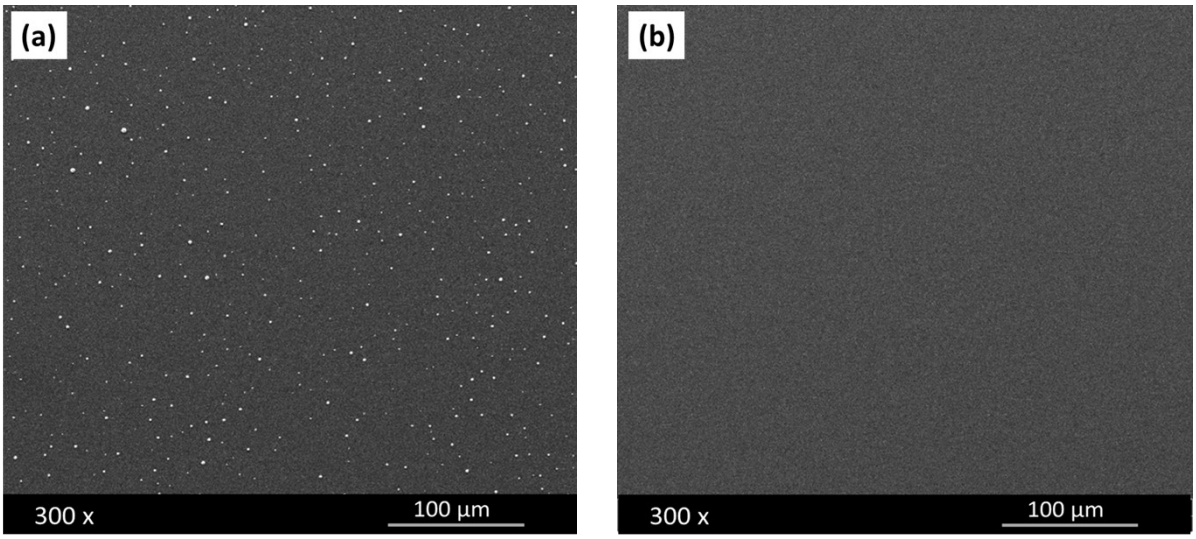

Figure S3: SEM observation of silicone SYLGARD184 (S184) after airbrush deposition of a control solution of CMC at 1 mg/mL (a) before and (b) after cleaning by immersion in water (2-min bath sonication).

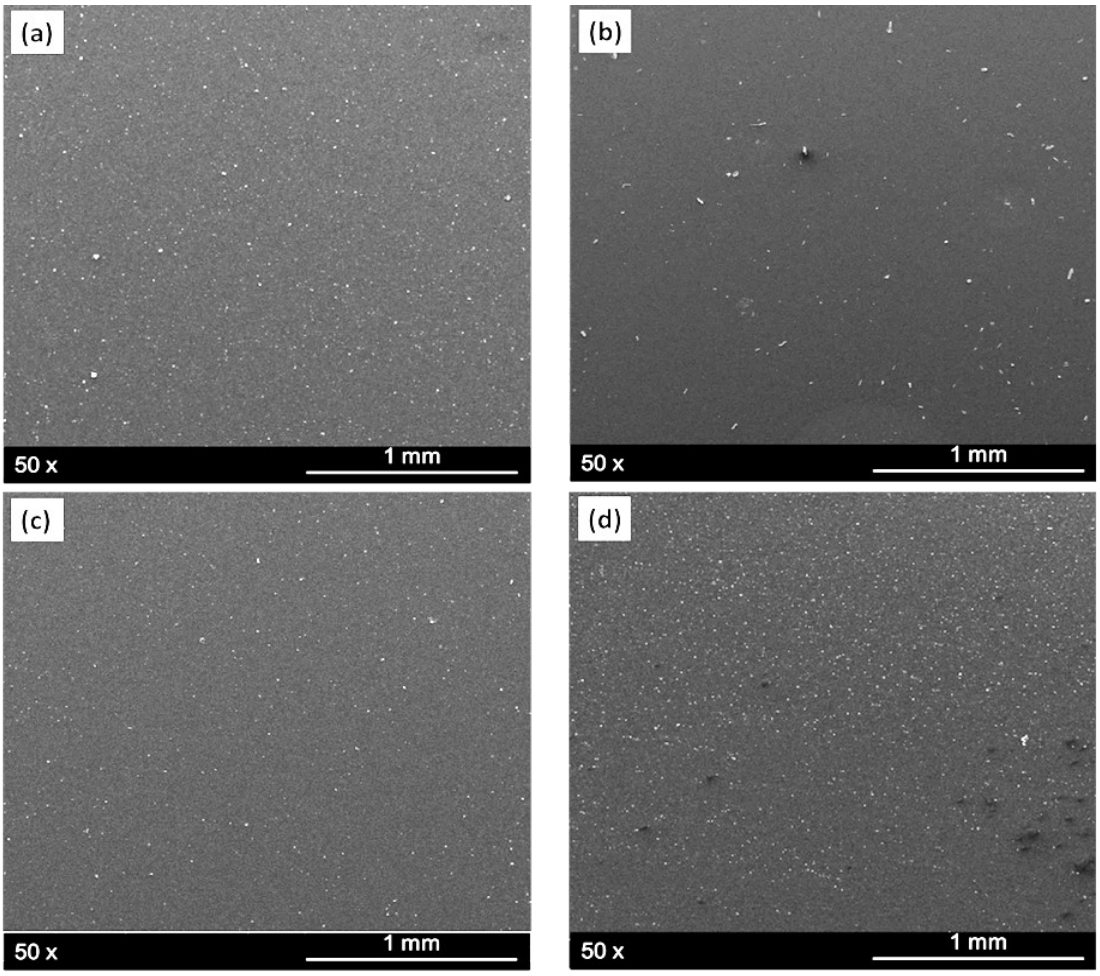

Figure S4a: SEM observation of CNMs on silicone materials: (a) DWCNTs; (b) DWCNTs Ox; (d) FLG; (f) GO on silicone S184, evidencing the rather homogeneous deposition achieved by airbrush deposition.

Series of figures S4b (below) illustrate the influence of some experimental parameters of spray deposition to discuss about the possible implantation of CNMs at the surface of the silicone.

The pressure of the air compressor itself cannot be tuned (kept constant between 2.5 to 3 bars on the model we are using), so it was not possible to investigate the influence of this parameter in this work. However, it is possible to tune the flow rate when gradually increasing the turns on the fluid control knob. Looking at the ink deposited on the silicone surface using an optical microscope, the CNM spots appear to increase in diameter, and these spots remain visible after 2 min in a sonication bath (see series of images below, in the case of DWCNT-OX as an example). This confirms that the CNMs are attached to the surface and their quantity can be empirically controlled. The number of turns was optimized to ensure a deposit of CNMs in all cases, in the same air-brushing conditions. Although the different silicones are fully polymerized in our work conditions according to the recommendations of the providers, it is likely that this may not be totally the case. We have found (not shown in the manuscript) that for shorter polymerisation times prior to spray deposition, CNMs may "sink" in the silicone, exhibiting only a very smooth surface topography, with no clearly protruding CNM. The fact that the CNMs are still present at the surface after mild sonication in a bath is additional convincing evidence that the CNMs are indeed anchored at the surface.

Bare Silicone MED4917 Surface	
X200	X1000
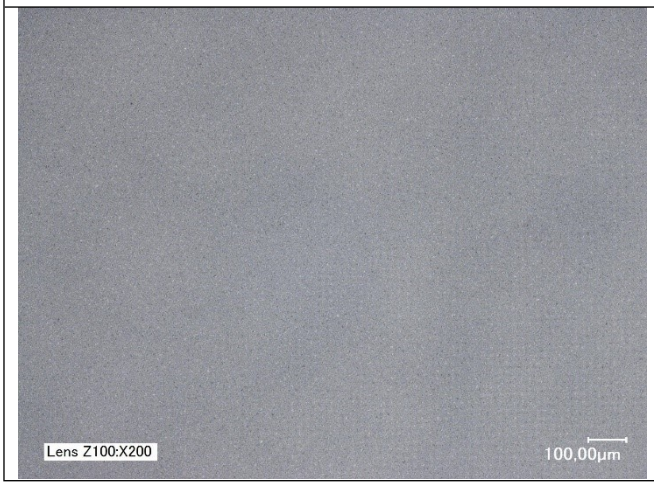	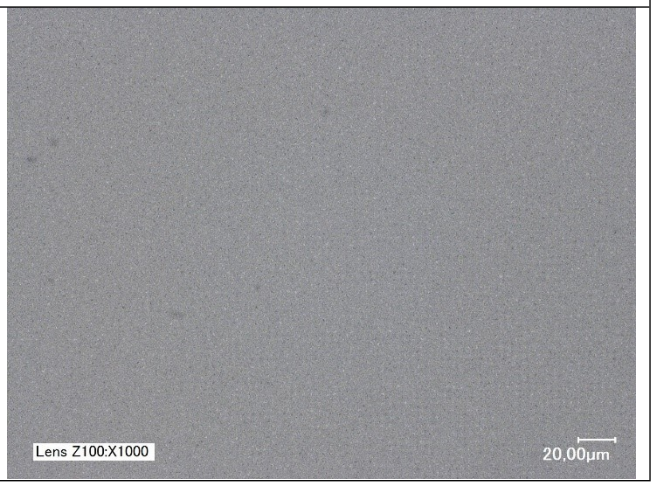

DWCNT-OX Treated Silicone MED4917 Surface – 3 turns	
No sonication bath	
X200	X1000
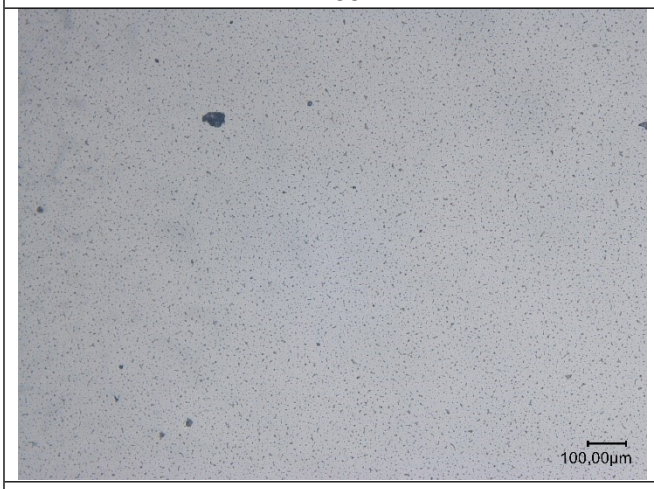	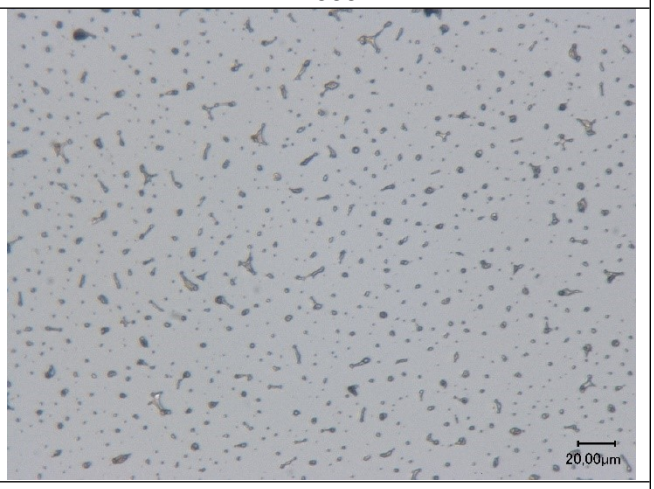
After 2 min sonication bath	
X200	X1000
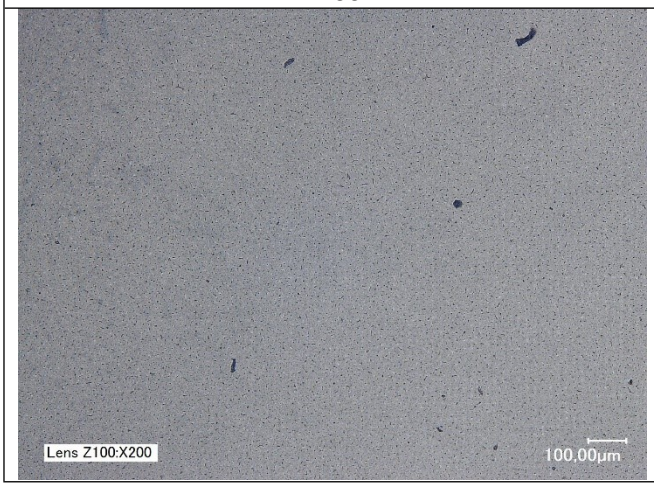	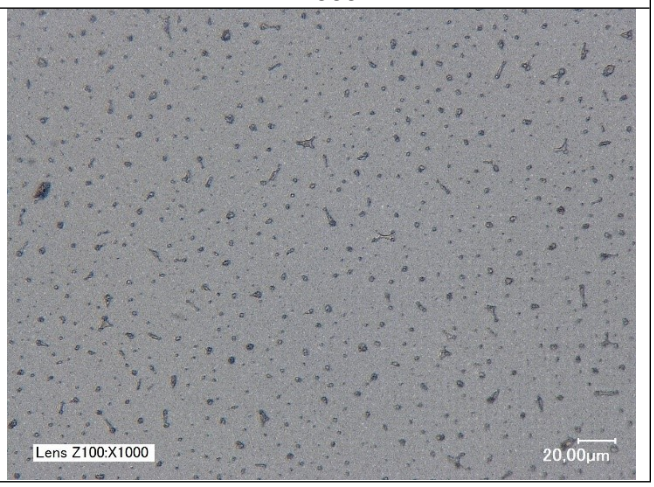

DWCNT-OX Treated Silicone MED4917 Surface – 5 turns	
No sonication bath	
X200	X1000
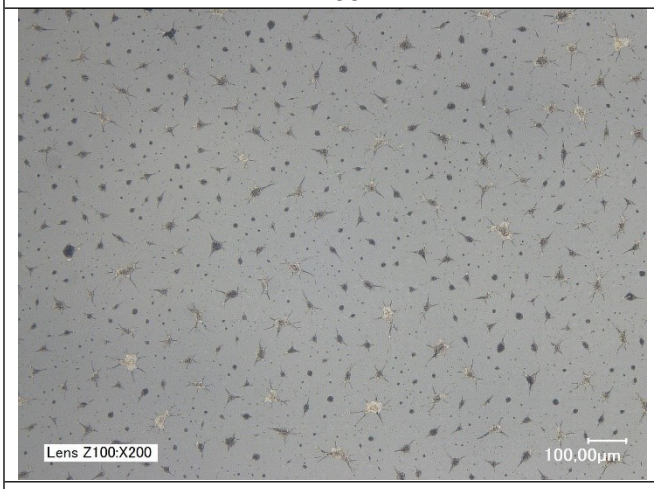	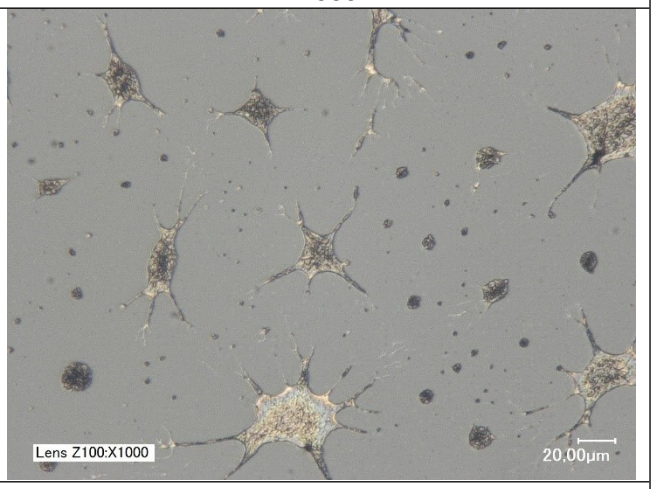
After 2 min sonication bath	
X200	X1000
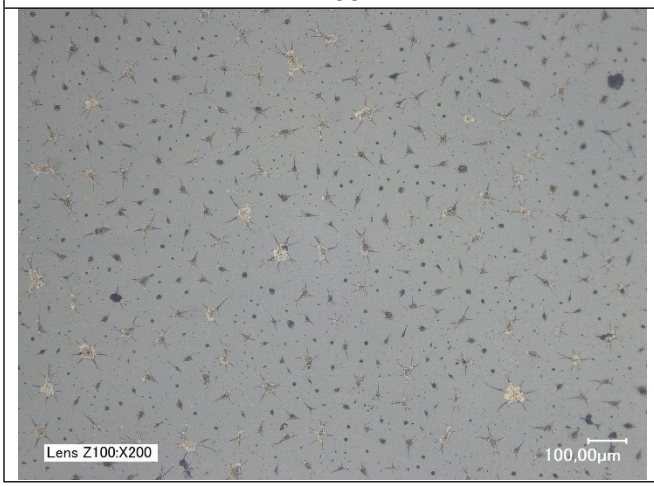	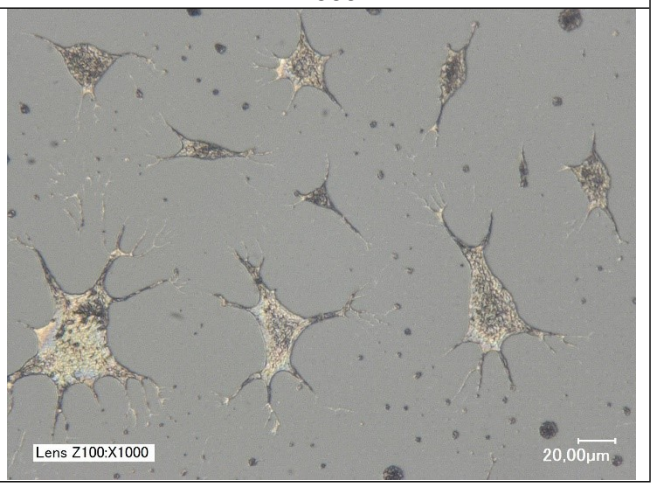

DWCNT-OX Treated Silicone MED4917 Surface – 10 turns	
No sonication bath	
X200	X1000
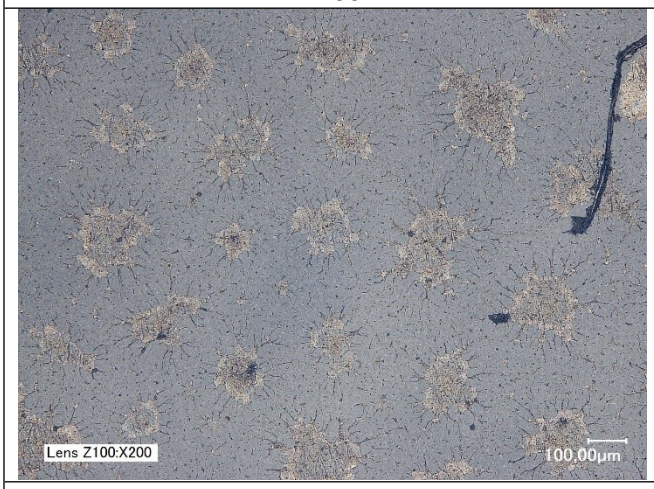	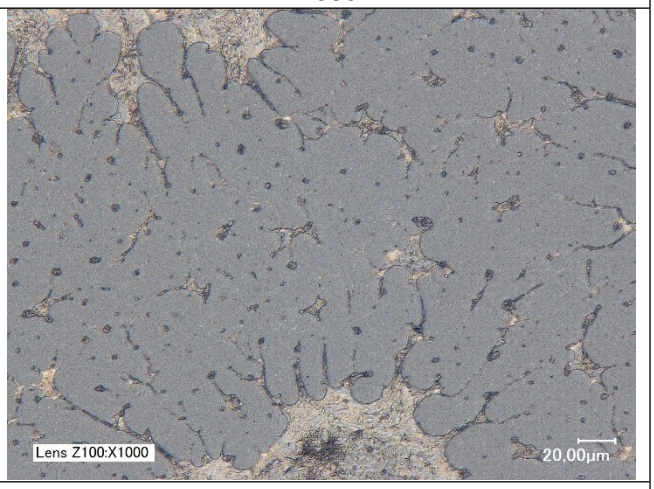
After 2 min sonication bath	
X200	X1000
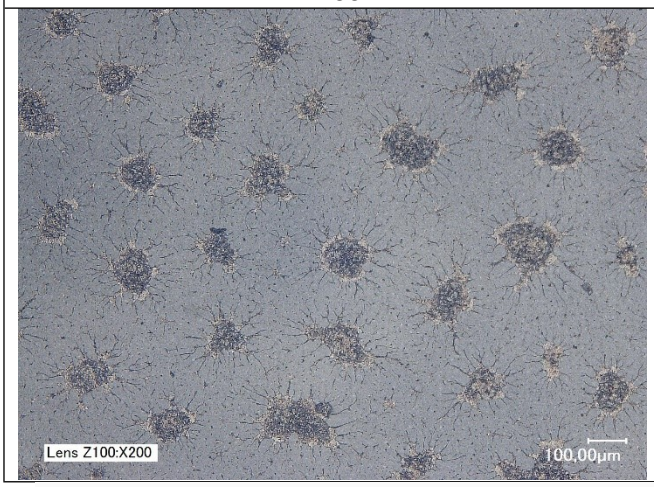	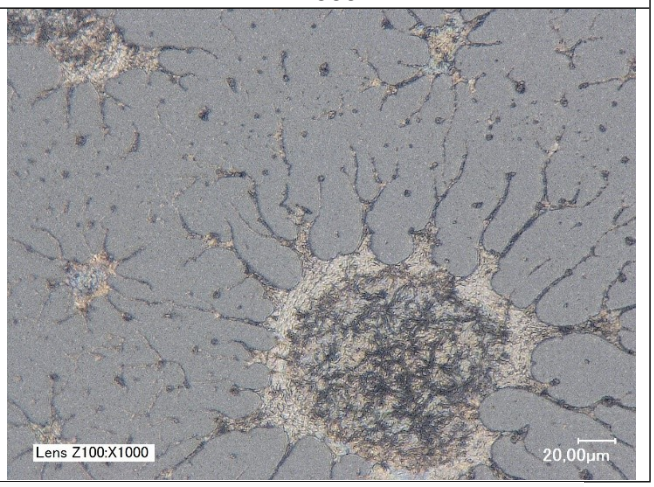

Figures S4b; this series of images compares deposits on MED4917 silicone with different air flows, controlled by the number of "turns" of the admission knob. We clearly evidence (i) that 2-min bath sonication does not remove the deposits, and (ii) that the diameter of the spots increases with the air flow, as expected.

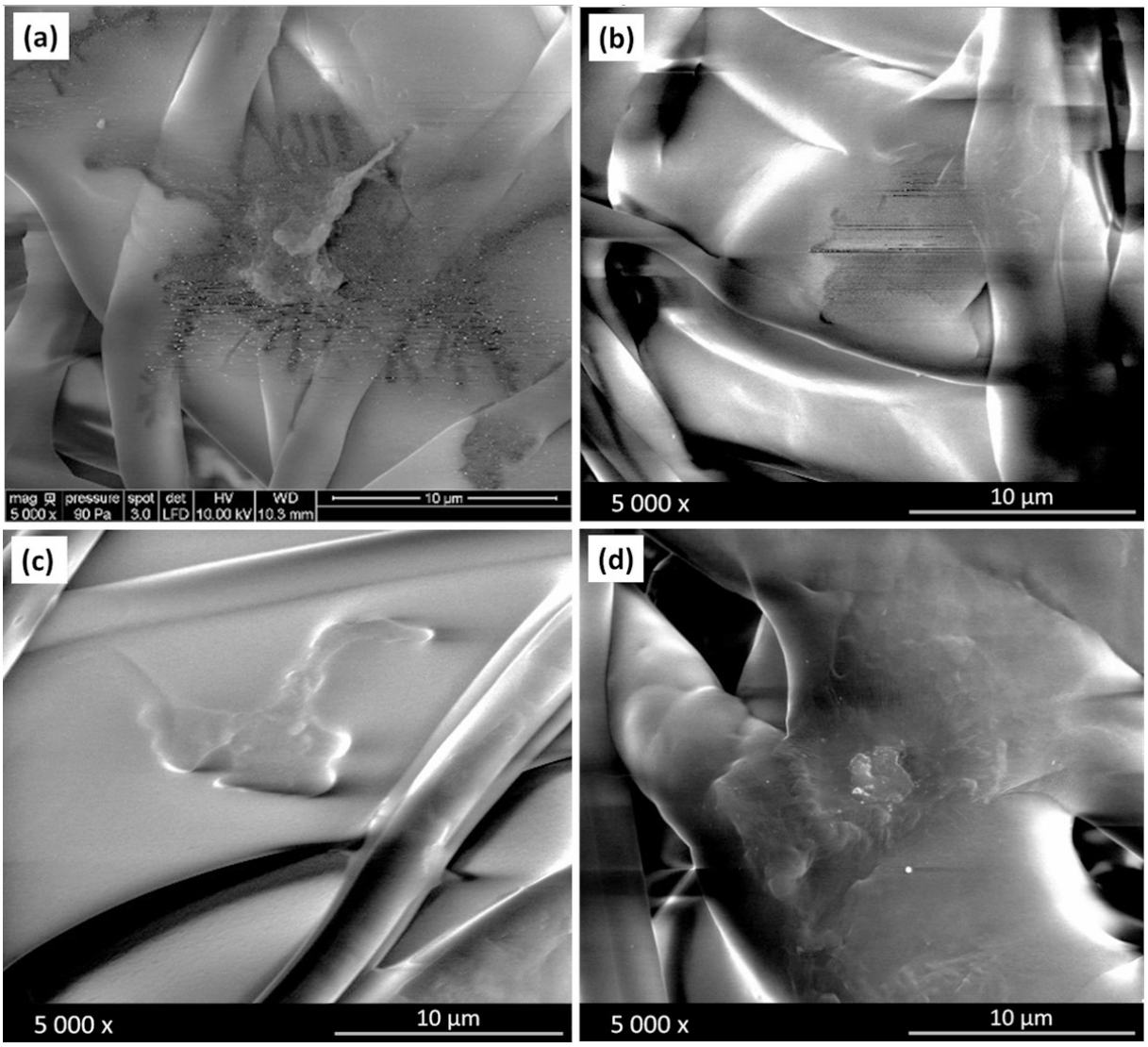

Figure S5: SEM observation of carbon nanoparticles deposited on classical FFP1 surgical mask tissue: (a) DWCNTs / mask ; (b) DWCNTs Ox / mask ; (c) FLG / mask ; (d) GO / mask.

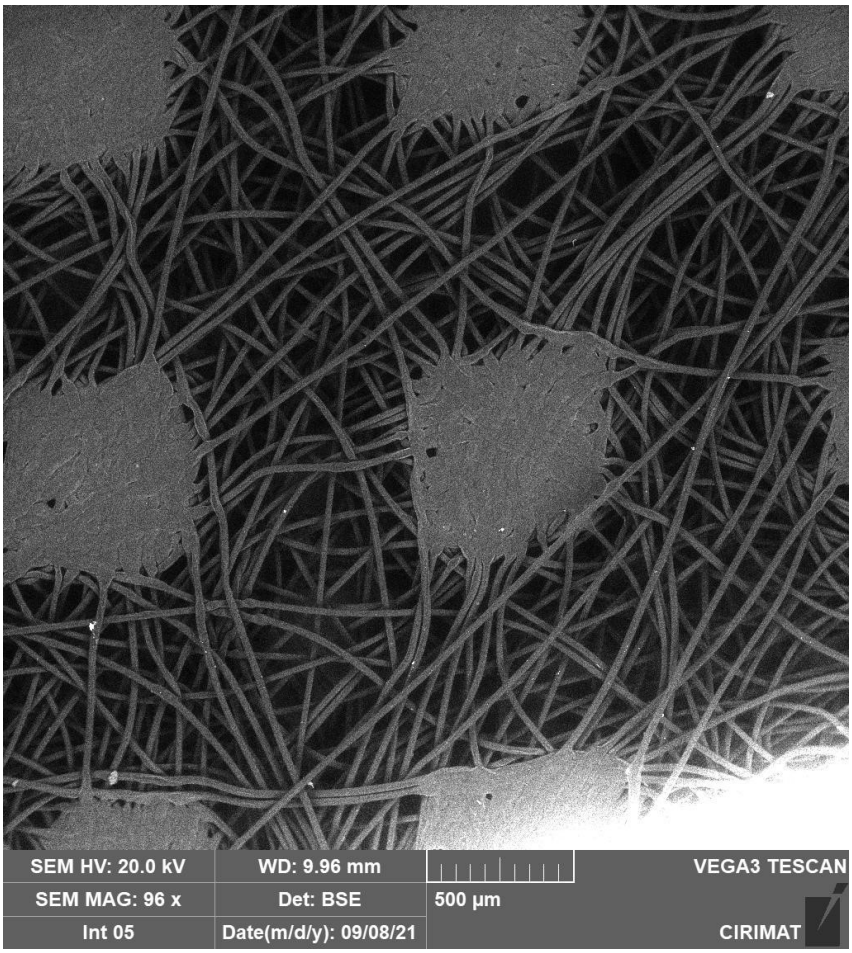

Figure S6: Low-magnification SEM image of the commercial graphene mask (graphene layer), showing the general organisation of the polymer fibres (graphene is not possible to observe at this scale).

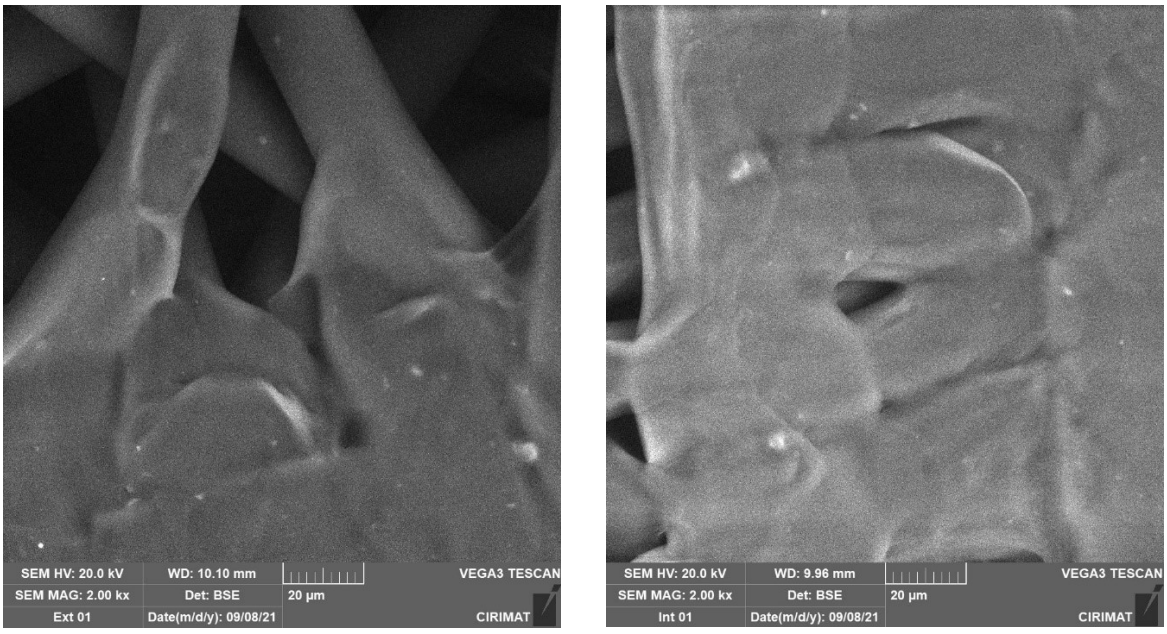

Figure S7: SEM observation of carbon nanoparticles on a commercial graphene mask.

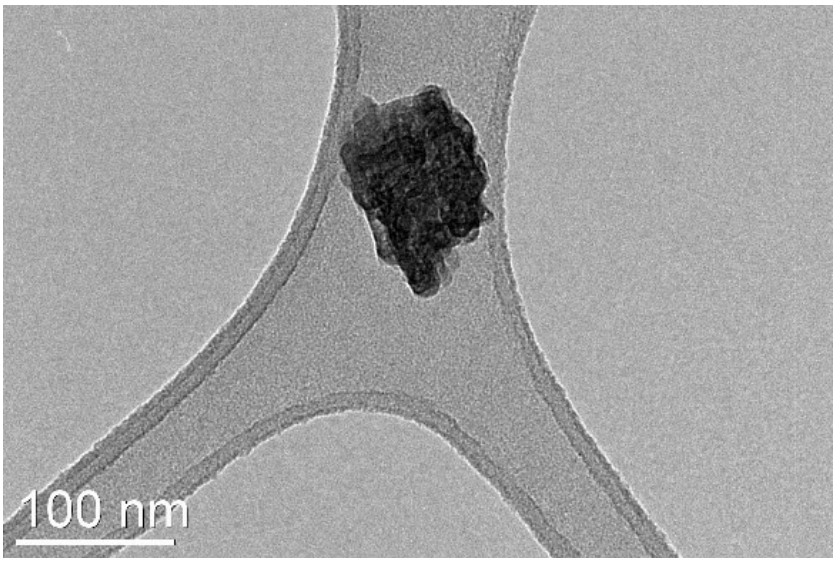

Figure S8: TEM observation of "*graphene material*" removed from the commercialized mask by bath sonication.

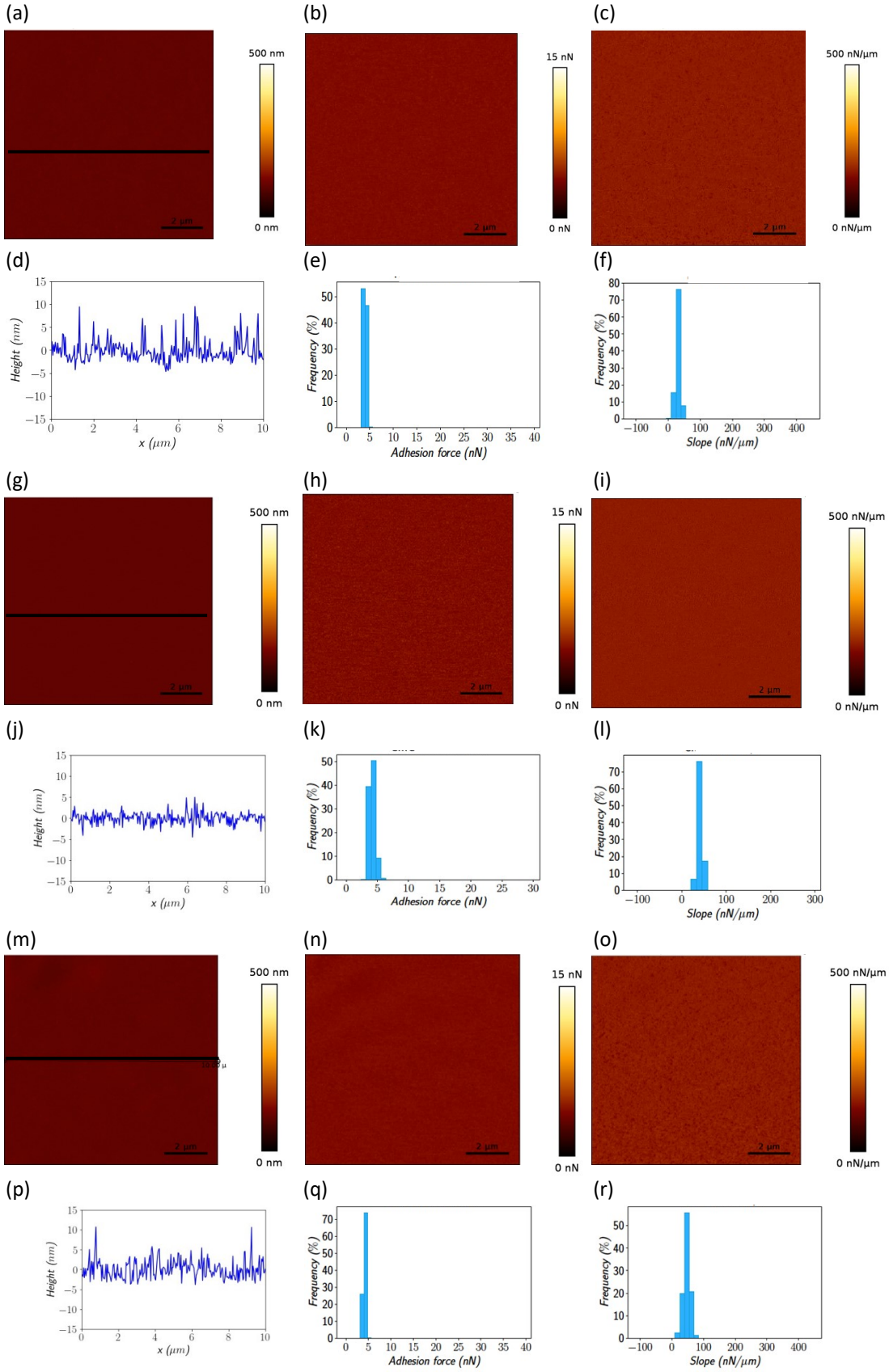

Figure S9: AFM multiparametric imaging (topography, adhesion and rigidity) of silicone MED control (a-f), CMC / S184 (g-l) and CMC / MED (m-r): (a, g, m) height maps; (b, h, n) adhesion maps; (c, i, o) slope maps; (d, j, p) height cross-sections; (e, k, q) adhesion distribution histograms; (f, l, r) slope distribution histograms.

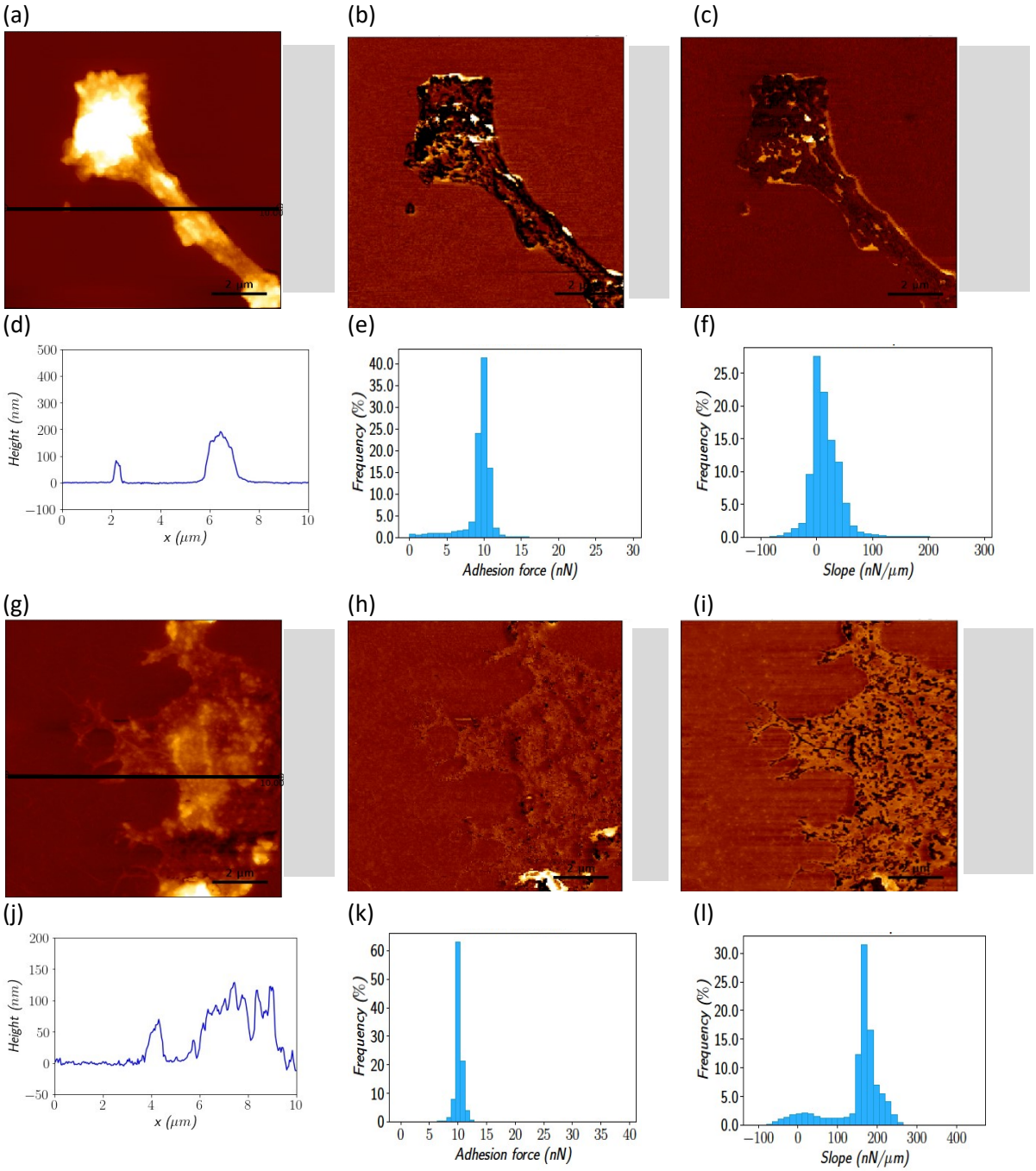

Figure S10: AFM multiparametric imaging (topography, adhesion and rigidity) of DWCNTs / S184 (a-f), and DWCNTs / MED (g-l): (a, g) height maps; (b, h) adhesion maps; (c, i) slope maps; (d, j) height cross-sections; (e, k) adhesion distribution histograms; (f, l) slope distribution histograms.

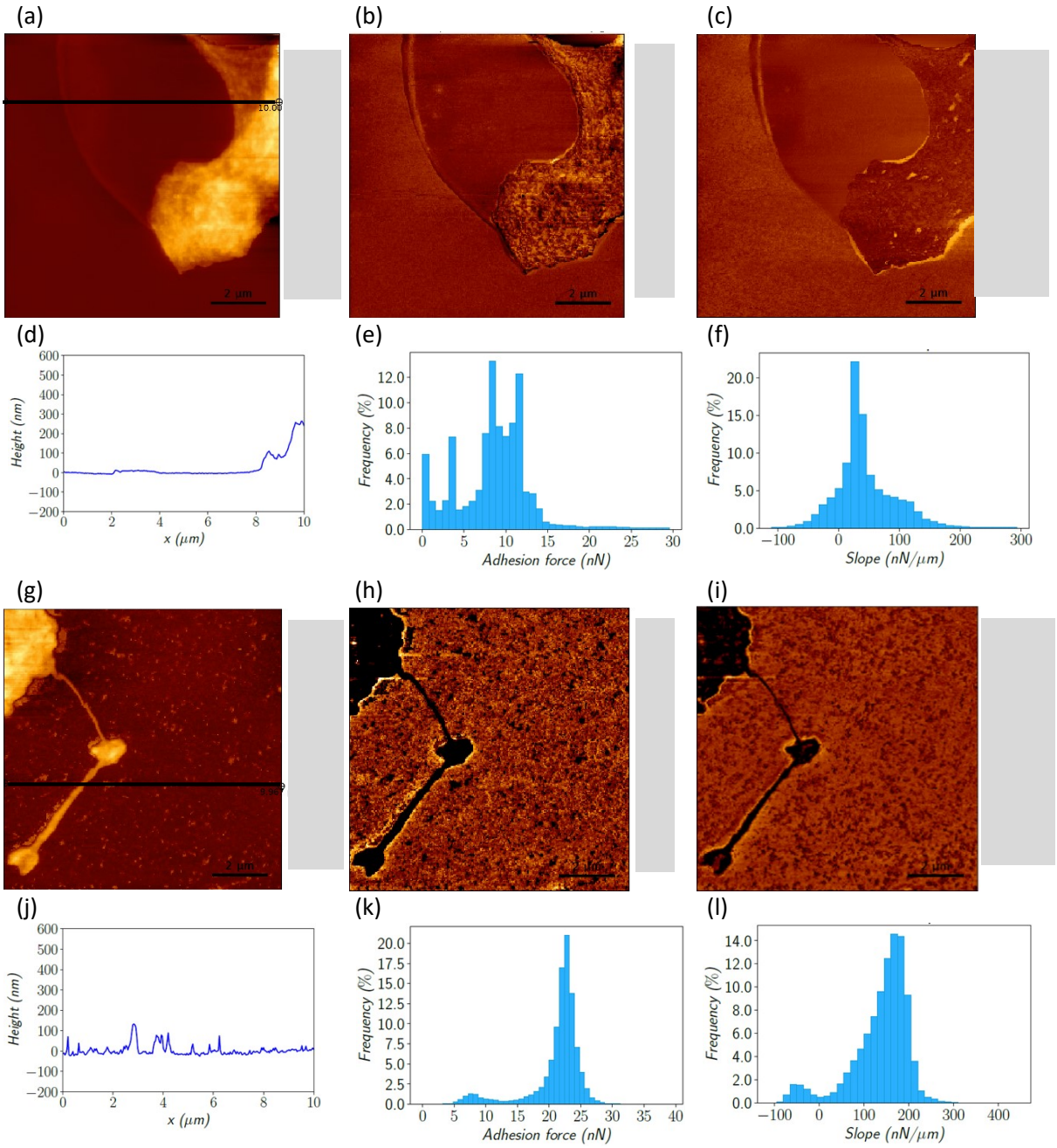

Figure S11: AFM multiparametric imaging (topography, adhesion and rigidity) of DWNTs Ox / S184 (a-f), and DWNTs Ox / MED (g-l): (a,g) height maps; (b, h) adhesion maps; (c, i) slope maps; (d, j) height cross-sections; (e, k) adhesion distribution histograms; (f, l) slope distribution histograms.

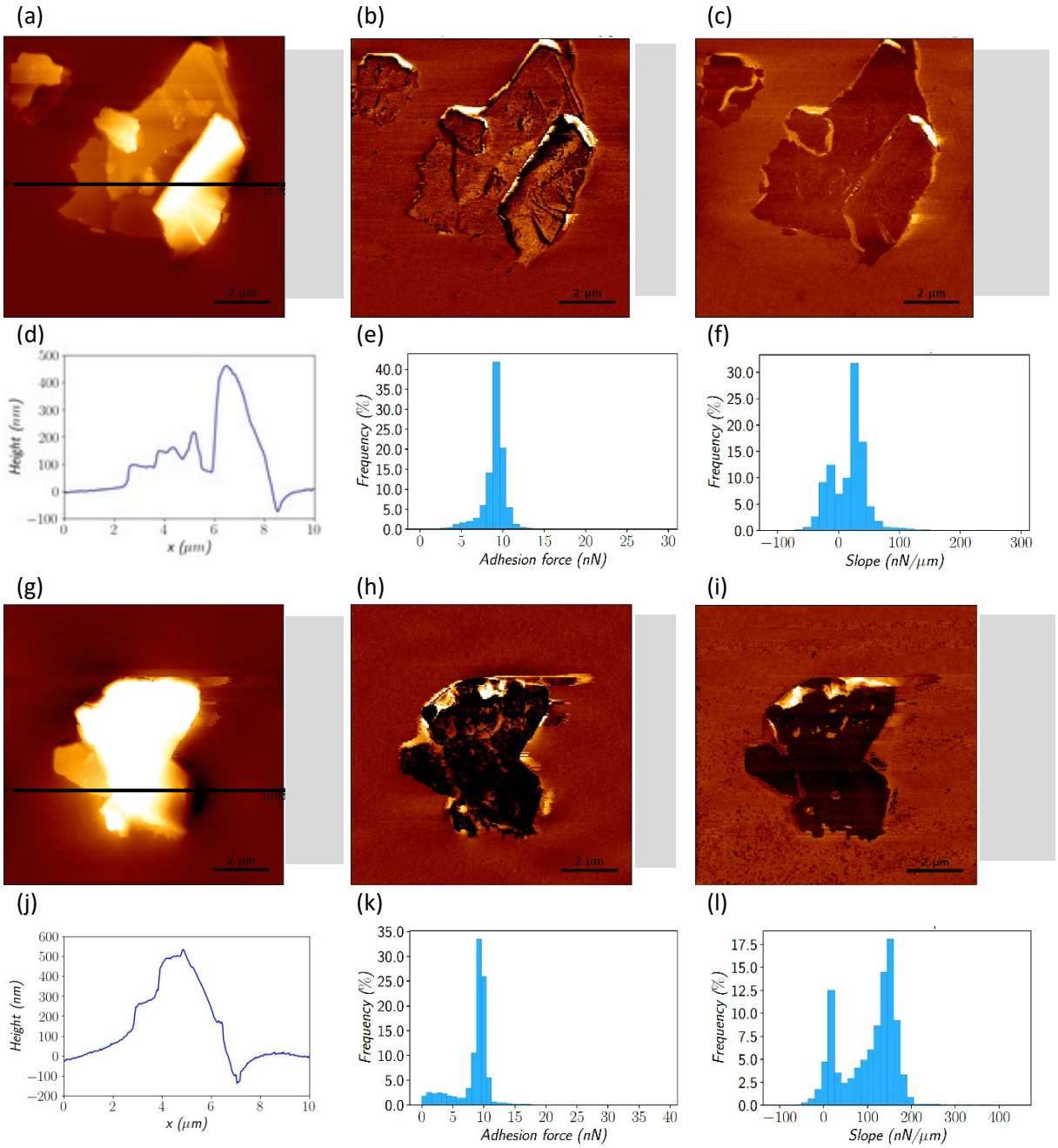

Figure S12: AFM multiparametric imaging (topography, adhesion and rigidity) of FLG / S184 (a-f), and FLG / MED (g-l): (a, g) height maps; (b, h) adhesion maps; (c, i) slope maps; (d, j) height cross-sections; (e, k) adhesion distribution histograms; (f, l) slope distribution histograms.